RSC Advances

PAPER

View Article Online
View Journal | View Issue

Cite this: *RSC Adv.*, 2022, **12**, 8792

Hygroscopic additive-modified magnesium sulfate thermochemical material construction and heat transfer numerical simulation for low temperature energy storage

Shi-Jie Li, *[ab] Xiang-Yu Yang,[c] Li-Sheng Deng,[d] Yong-Chun Fu,[a] Ming-Jun Pang,[a] Ti Dong,[b] Yi-Song Yu,[b] Ling-Na Su[a] and Shang Jiang*[a]

In this research, the core objective is to explore the effect of super-absorbent polymer material (poly(sodium acrylate)) on the heat storage performance of magnesium sulfate and to investigate the heat transfer behavior of 13X-zeolite, nano-aluminum oxide (nano-Al_2O_3) and poly(sodium acrylate) modified magnesium sulfate in a reactor. Finally it provides support for future material and reactor design. All characterizations and performance tests were done in the laboratory and a numerical simulation method was used to investigate the heat transfer behavior of the reactor. Through hydrothermal treatment, bulk $MgSO_4 \cdot 6H_2O$ was changed into nanoparticles (200–500 nm) when composited with poly(sodium acrylate), 13X-zeolite and nano-Al_2O_3. Among these materials, $MgSO_4 \cdot 6H_2O$ shows the highest activation energy (36.8 kJ mol^{-1}) and the lowest energy density (325 kJ kg^{-1}). The activation energy and heat storage energy density of nano-Al_2O_3 modified composite material MA-1 are 28.5 kJ mol^{-1} and 1305 kJ kg^{-1}, respectively. Poly(sodium acrylate) modified composite material, MPSA-3, shows good heat storage energy density (1100 kJ kg^{-1}) and the lowest activation energy (22.3 kJ mol^{-1}) due its high water-absorbing rate and dispersing effect. 13X-zeolite modified composite material MZ-2 shows lower activation energy (32.4 kJ mol^{-1}) and the highest heat storage density (1411 kJ kg^{-1}), which is 4.3 times higher than that of pure magnesium sulfate hexahydrate. According to the heat transfer numerical simulation, hygroscopic additives could prominently change the temperature distribution in the reactor and efficiently release heat to the thermal load side. The experimental and numerical simulation temperatures are similar. This indicates that the result of the numerical simulation is very close to the actual heat transfer behavior. This reactor could output heat at around 50 °C and absorb heat in the range of 100–200 °C. All these results further prove the strategy that thermochemical nanomaterial synthesis technology combined with material-reactor heat transfer numerical simulation is feasible for future material and reactor design.

Received 17th January 2022
Accepted 8th March 2022

DOI: 10.1039/d2ra00344a

rsc.li/rsc-advances

1. Introduction

The storage of waste heat or solar energy is an important way to promote the utilization efficiency of renewable and sustainable energy and reduce the consumption of fossil fuels. In achieving this target, various materials with high storage capacity based on the matching system have been designed.[1,2] These technologies can commonly be divided into three main types: sensible heat storage,[3,4] latent heat storage[5,6] and thermochemical heat storage.[7–11] However, the first two technologies can more easily lose conserved thermal energy, and are therefore not appropriate candidates for long-term heat storage.[12] Among these technologies, thermochemical heat storage using a reversible chemical reaction with thermal energy change to release and store heat shows the highest efficiency for thermal energy utilization because of its excellent heat storage density.[13] Large numbers of materials could thus be researched for use in thermochemical heat storage over a wide range of working temperatures.[12–19] Kubota *et al.*[9,20] composed a porous carbon and hygroscopic material with lithium hydroxide (LiOH) for low-temperature energy storage and the heat storage performance was obviously improved. This research proves that

---

[a] *Institute of Carbon Materials Science, Shanxi Datong University, Datong, 037009, P. R. China. E-mail: jiangshang3714@163.com*

[b] *Key Laboratory of Renewable Energy, Guangdong Provincial Key Laboratory of New and Renewable Energy Research and Development, Guangzhou Institute of Energy Conversion, Chinese Academy of Sciences, No. 2 Nengyuan Rd., Wushan, Tianhe District, Guangzhou 510640, P. R. China*

[c] *School of Materials Science and Engineering, Taiyuan University of Technology, Taiyuan, 030024, P. R. China*

[d] *Guangdong Intelligent Filling Technology Limited Company, No. 63 (F3) 5, Zone C, Sanshui Industrial Park, Foshan, Guangdong, 528137, P. R. China*

additive materials could enhance the performance and the heat and mass transfer property of the materials. Pierrès and other researchers[21] studied the heat and mass transfer mechanism of the hydrated salt strontium chloride monohydrate ($SrCl_2 \cdot H_2O$) in an open reactor system. The finite element method was used to construct a two-dimensional model of the reactor. Their results indicate that the water steam partial pressure and reactor inlet pressure have a tremendous influence on the thermal energy storage behavior. Mass transfer is the main parameter for controlling the performance of the open reactor. Malley-Ernewien *et al.*[22] showed the influence of heat and mass transfer properties, such as pressure loss and temperature distribution, on the construction of a chemical heat storage reactor. This study shows that an increasing number of reaction beds and increasing bed compactness favour an improvement in the performance of a thermal energy storage reactor. Luo *et al.*[23] listed summaries of the advantages and prospects of salt hydrate thermochemical energy storage, especially metal–organic framework (MOF) materials that are used for salt hydrate-based thermal energy storage. They also showed the importance of heat and mass transfer in the materials and the reactor. For the sake of efficiently recycling low-temperature thermal energy at around 150 °C, inorganic hydrate magnesium sulfate heptahydrate ($MgSO_4 \cdot 7H_2O$) was selected. It is considered to be an excellent heat storage material for low-temperature thermal energy utilization. It is also non-toxic, low-cost and non-corrosive with potential for green energy applications in buildings. The endothermic/exothermic reaction of magnesium sulfate is also related to magnesium sulfate ($MgSO_4$) and water vapour in the atmosphere with high relative humidity and the release of chemical energy. But, the reaction cannot be fully completed.[24] When $MgSO_4$ and water are stored separately, the former thermal energy, which has been converted to chemical bond energy, could be stored long-term.

In order to improve the heat storage performance of $MgSO_4$, many researchers have done a lot of work. Posern and Kaps[18] found that when magnesium chloride ($MgCl_2$) was added into $MgSO_4$, the water sorption behavior of these binary composite heat storage materials was greatly changed. $MgCl_2$ partially replaced $MgSO_4$ to reduce the deliquescence relative humidity of the mixture, so as to increase the condensation capacity and energy density. But, meanwhile, the chlorides presented certain corrosivity. Therefore, the mixed ratio of these two salts should be well controlled. Ata Ur Rehman *et al.*[25] prepared an $MgSO_4$/$ZnSO_4$ (zinc sulfate) composite material and investigated its heat storage performance. The result showed that the energy density and water adsorption amount of this binary composite were notably enhanced. This may be due to the optimal mixed ratio and better adsorption property compared to each single salt. Hongois *et al.*[26] used zeolite as an additive for a magnesium sulfate heat storage material. And the heat storage performance was obviously improved. $MgSO_4$ could be well dispersed on the zeolite surface due to its porous expanded structure. This type of structure also benefited the thermal energy release and absorbance. Xu *et al.*[27] investigated the hydration behavior of zeolite–$MgSO_4$ composites for heat storage. They found that zeolite–$MgSO_4$ materials showed higher heat storage performance and hydration ability than pure zeolite. But the hydration ability greatly decreased when the temperature was higher than 50 °C. It can be seen from the above research that magnesium sulfate hydrate materials still have many shortcomings which need to be solved. Similar to other inorganic hydrates,[28] both the heat and mass transfer and reaction performance of magnesium sulfate hydrate materials are poor,[24] which severely restricts the commercial application of magnesium sulfate heptahydrate for heat storage. Consequently, a heat storage material based on $MgSO_4$ with excellent water vapor uptake and high thermal conductivity urgently needs to be developed. 13X-zeolite, nano-aluminum oxide and a super-absorbent polymer material, which in this research is poly(sodium acrylate), are chosen as hygroscopic additives for thermal energy utilization. 13X-zeolite and nano-aluminum oxide as excellent porous materials are always used for gas separation, for instance, volatile organic chemicals,[29] carbon dioxide,[30] catalysts[31] and solar cells,[32] due to their excellent adsorption property and porosity. The super-absorbent polymer (SAP) material, poly(sodium acrylate), has a strong adsorption effect on neighbouring water molecules and is always used for sewage treatment and electrics.[33,34]

In this work, due to the instability of $MgSO_4 \cdot 7H_2O$ at room temperature and atmospheric pressure, it is necessary to heat it to produce stable magnesium sulfate hexahydrate ($MgSO_4 \cdot 6H_2O$). Meanwhile, the super-absorbent polymer material, poly(sodium acrylate), has rarely been researched for thermochemical heat storage. The heat transfer behavior of poly(sodium acrylate), porous 13X-zeolite and nano-Al_2O_3 modified magnesium sulfate in a reactor is not yet well known. Therefore, in order to develop new heat storage materials and further improve reactor design, four types of thermochemical materials were prepared. The heat storage performance was investigated and the heat transfer behavior of the materials in the reactor was numerically simulated.

2. Experimental

2.1 Materials and methods

The thermochemical materials were prepared by a hydrothermal method using $MgSO_4 \cdot 7H_2O$ (Aladdin, Ltd, purity 99.0%) as the raw material and poly(sodium acrylate) (Shengli Oil Field Changan Group, purity >98.0%), 13X-zeolite (Damao Chemical Reagent Factory, purity 98.0%) and nano-Al_2O_3 (Aladdin, Ltd, purity 99.9%) as hygroscopic additives. Firstly, $MgSO_4$ solution was prepared by slowly adding 1186 mg of $MgSO_4 \cdot 7H_2O$ into 10 mL of DI water under strong stirring at 25 °C for 5 min and then moved into a 20 mL stainless steel hydrothermal reactor. After that, 785 mg of poly(sodium acrylate) was placed into the reactor also under stirring for 1 h. Finally the reactor was heated to 150 °C and kept there for 8 h. During the hydrothermal process, due to the increase in temperature and pressure in the hydrothermal reactor, the solubility of the materials starts to decrease and reach saturation, and they precipitate from the solution in a crystalline form of the compound type. The materials generate corresponding coordination aggregates through hydrolysis and polycondensation. When the concentration reaches supersaturation, the materials begin to precipitate many crystal nuclei and finally grow into small crystals. By controlling the hydrothermal temperature and time, further growth of crystalline particles is limited and a large number of nanoparticles are eventually formed around the crystal nuclei. Meanwhile, because of the uniform contact between additives and $MgSO_4$ solution, nanoparticles could easily be generated and well dispersed on the additive materials. When the obtained material had cooled to room temperature, it was dried at 150 °C for 2 h in a horizontal tubular quartz furnace under Ar buffer gas. After that the material temperature was reduced to 30 °C and it was reacted with water vapor carried with N_2 flow gas for 30 min. Then all the samples were heated to 40 °C for 24 h, and finally the target products were obtained. All the samples were prepared using the same method. Definitions of the names of the four obtained materials are listed in Table 1. A large number of products were synthesized and collected, which were dried at 150 °C for 2 h. After that the obtained materials (700 g) and water vapor flow were loaded in a stainless-steel cylindrical reactor (ϕ 100 mm × h 300 mm × w 2 mm) at 30 °C. It was equipped with four K-type thermocouples, located at the center, the inner wall, upper surface and lower surface of the materials in the reactor. These thermocouples were used to test the temperature (T_c, T_w, T_{su}, T_{sl}) of the above-mentioned four positions, as shown in Fig. 1a.

After 30 min the values of the temperatures of T_c, T_w, T_{su} and T_{sl} of the four materials were recorded. These experimental temperature values were used as a reference for a comparison with the numerical simulation temperatures to verify their correctness (Fig. 8).

2.2 Characterization and performance testing

The microstructure was measured by field-emission scanning electron microscopy (SEM, S-4800, Hitachi Limited). X-ray diffraction (XRD) analysis was performed on a D8-Advance X-ray diffractometer (Bruker, Germany) with a Cu target (40 kV, 40 mA). Nitrogen adsorption–desorption was measured at the boiling point of nitrogen (77 K) using a Quantachrome QDS-30 analyzer. The BET surface area and pore structure were measured by nitrogen physisorption under a normal relative pressure of 0.1–1.0. The thermal conductivity of the samples was measured by a TPS2500S thermal conductivity tester (Hot Disk, Sweden). The water vapor adsorption properties were tested using a constant-temperature-and-humidity test box (YNK/TH-150, Suzhou UNIQUE Environmental Test Equipment, China). The energy and mass change of the samples were measured with an STA-449F5 simultaneous thermal analyzer (Netzsch Co., Ltd, Germany). The activation energies of the dehydration reaction of all the samples were calculated by the Kissinger method.[35] According to this method, the following equation can be obtained based on the reaction rate expression and Arrhenius's equation:

$$\ln\left(\frac{\beta}{T^2}\right) = \ln\frac{R}{E}\frac{A}{f(\alpha)} - \frac{E}{R}\frac{1}{T} \tag{1}$$

In this equation, E is the activation energy [kJ mol^{-1}], β is the heating rate [K min^{-1}], T is the peak temperature [K], R is the molar gas constant [J (mol$^{-1}\cdot$K^{-1})], A is a pre-exponential factor, α is the dehydration conversion and $f(\alpha)$ is a function of dehydration conversion, which here takes a fixed value. During the calculation of activation energy, the heating rates were 5 K min^{-1}, 10 K min^{-1}, 15 K min^{-1} and 20 K min^{-1}, and the activation energy was obtained from the slope ($-E/R$) of this equation.

Table 1 Definition of the names of hygroscopic nanoadditive modified magnesium sulfate based thermochemical materials

Sample name	Materials composition
MA-1	$MgSO_4\cdot 6H_2O/Al_2O_3$
MZ-2	$MgSO_4\cdot 6H_2O$/13X-zeolite
MPSA-3	$MgSO_4\cdot 6H_2O$/poly(sodium acrylate)
$MgSO_4\cdot 6H_2O$	$MgSO_4\cdot 6H_2O$

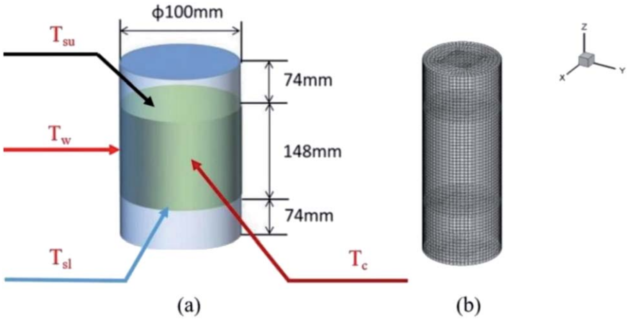

Fig. 1 (a) The physical model and (b) heat transfer 3D numerical grid of the reactor with heat storage materials.

2.3 Heat transfer numerical simulation of a magnesium sulfate based composite heat storage material in reactor

For the heat transfer numerical simulation, commercial computational fluid dynamics (CFD) software, fluent, which is based on the finite volume approximation method, was selected and used. Firstly, a stainless-steel cylindrical reactor with a bottom internal diameter of 100 mm, height of 300 mm and wall thickness of 2 mm was constructed as a physical model (Fig. 1a). As shown in Fig. 1a, T_c and T_w stood for the core temperature and inner wall temperature, respectively, of the reactor filled with heat storage material. T_{sl} and T_{su} were the lower surface and upper surface temperature, respectively, of the heat storage material in the reactor. After building the physical model, the heat transfer behavior was simulated according to the hydration reaction in the reactor. A cylindrical reaction region with nitrogen and reactants as a whole system was established (Fig. 1b). The governing equation of the air domain is eqn (2) and the governing equation for the sample region is eqn (3), where ρ is the gas density, kg m^{-3}; C_p is the specific heat capacity, J kg^{-1} K^{-1}; T is the temperature, K; t is the time, s; k is the thermal conductivity coefficient, W m^{-1} K^{-1};

$$\rho_{\text{air}} c_{\text{p-air}} \frac{\partial T}{\partial t} = \frac{1}{r}\frac{\partial}{\partial r}\left(k_{\text{air}} r \frac{\partial T}{\partial r}\right) + \frac{1}{r^2}\frac{\partial}{\partial \varphi}\left(k_{\text{air}} \frac{\partial T}{\partial \varphi}\right) + \frac{\partial}{\partial z}\left(k_{\text{air}} \frac{\partial T}{\partial z}\right) \quad (2)$$

$$\rho_{\text{sample}} c_{\text{p-sample}} \frac{\partial T}{\partial t} = \frac{1}{r}\frac{\partial}{\partial r}\left(k_{\text{sample}} r \frac{\partial T}{\partial r}\right) + \frac{1}{r^2}\frac{\partial}{\partial \varphi}\left(k_{\text{sample}} \frac{\partial T}{\partial \varphi}\right) + \frac{\partial}{\partial z}\left(k_{\text{air}} \frac{\partial T}{\partial z}\right) + Q_1 + Q_2 \quad (3)$$

Q_1 is the chemical reaction heat of the sample, W m^{-3}, and Q_2 is the built-in heating source of the reactor, W m^{-3}. The composite boundary conditions of the whole heat transfer region are as follows:

$$-k_{\text{air}}\left(\frac{\partial T}{\partial r}\right)_{r=R} = h(T - T_{\text{f}}) \text{ and } k_{\text{air}}\left(\frac{\partial T}{\partial r}\right)_{r=-R} = h(T - T_{\text{f}}) \quad (4)$$

$$-k_{\text{sample}}\left(\frac{\partial T}{\partial r}\right)_{r=R} = h(T - T_{\text{f}}) \text{ and } k_{\text{sample}}\left(\frac{\partial T}{\partial r}\right)_{r=-R} = h(T - T_{\text{f}}) \quad (5)$$

$$-k_{\text{shell}}\left(\frac{\partial T}{\partial r}\right)_{r=R} = \varepsilon\sigma\left(T^4 - T_{\text{f}}{}^4\right) \quad (6)$$

The initial conditions of the calculation are as follows:

$$T(r,t) = T_0, \text{ at } t = 0 \quad (7)$$

In order to speed up the convergence, the 1st-order upwind differencing scheme was used to discretize the spatial-derivative term. Meanwhile, a fully implicit scheme was employed to discretize the transient term. The heat sources were customized by using the user-defined functions (UDFs) available in FLUENT. The numerical elements of the samples and air regions were hexahedral. The numerical elements have a volume of about 1.10×10^{-8} m^3 to 1.16×10^{-8} m^3 and the total number of numerical meshes is 39552. Grid-independence tests were conducted to guarantee that the mesh employed gave calculation results of adequate accuracy.

3. Results and discussion

3.1 Microstructural characterization of magnesium sulfate based thermochemical materials

Fig. 2 shows the XRD spectra of the $MgSO_4 \cdot 6H_2O$, MA-1, MZ-2 and MPSA-3 samples. Table 2 shows the locations of the X-ray diffraction peak of the different materials observed in Fig. 2. The diffraction peaks at around 14.7° to 58.7° (Table 2) are attributed to $MgSO_4 \cdot 6H_2O$ (PDF# 24-0719). And the diffraction peaks at around 16.2° to 67.5° (Table 2) are assigned to Al_2O_3. 13X-zeolite could be identified in MZ-2 by six diffraction peaks at around 26.0°, 26.8°, 34.5°, 41.4°, 47.3° and 57.4° (Table 2). But there is no diffraction peak for poly(sodium acrylate) in sample MPSA-3. This may be because poly(sodium acrylate)the exists in a noncrystalline state, and in XRD characterization, only crystals have a diffraction effect on X-rays. As shown in Fig. 2, the high-strength diffraction peaks of pure $MgSO_4 \cdot 6H_2O$ are sharp and strong. Meanwhile, comparing the intensity of diffraction peaks of $MgSO_4 \cdot 6H_2O$ in the composite materials (MA-1, MZ-2, MPSA-3), it was found that the diffraction intensity was similar to those of $MgSO_4 \cdot 6H_2O$ in MZ-2 and MPSA-3. The intensities of the $MgSO_4 \cdot 6H_2O$ diffraction peak of these two composite materials were slightly lower than that in MA-1. And in all these composite materials, the intensity of the $MgSO_4 \cdot 6H_2O$ diffraction peak was significantly weaker than that of pure $MgSO_4 \cdot 6H_2O$. This indicates the successful and good dispersion of $MgSO_4 \cdot 6H_2O$ in the composite materials.

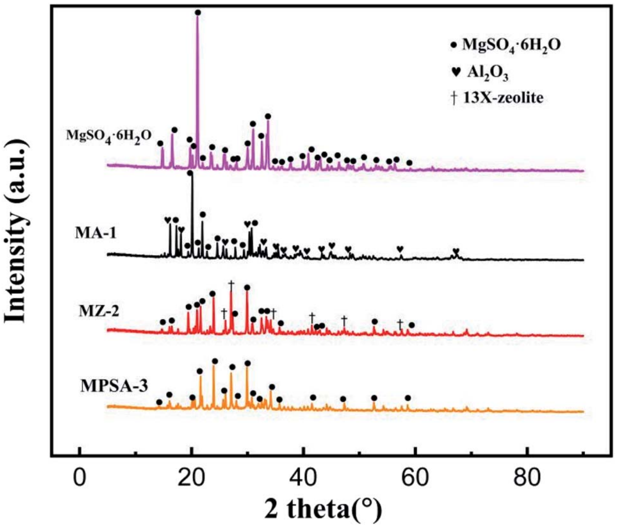

Fig. 2 XRD patterns of thermochemical heat storage materials composed of $MgSO_4 \cdot 6H_2O$, MA-1 ($MgSO_4 \cdot 6H_2O/Al_2O_3$), MZ-2 ($MgSO_4 \cdot 6H_2O$/13X-zeolite) and MPSA-3 ($MgSO_4 \cdot 6H_2O$/poly(sodium acrylate)).

Fig. 3a–d provide the SEM images of thermochemical heat storage materials composed of $MgSO_4 \cdot 6H_2O$, MA-1, MZ-2 and MPSA-3. From the SEM characterization, a big bulk $MgSO_4 \cdot 6H_2O$ crystal existing in the form of stacked flakes (Fig. 3a) with a diameter of around 6 μm could be clearly seen. And after composition with Al_2O_3, 13X-zeolite and poly(sodium acrylate) (Fig. 3b–d), the minimum diameter of $MgSO_4 \cdot 6H_2O$ could reach 200–500 nm. $MgSO_4 \cdot 6H_2O$ particles were well dispersed according to the XRD results, but some parts of the hygroscopic additives, especially the surface (Fig. 3d), were covered. This may affect the heat and mass transfer property during the heat

Table 2 Location of X-ray diffraction peaks of the different materials observed in Fig. 2

Materials	Diffraction peak location/2θ°
$MgSO_4 \cdot 6H_2O$	14.7°, 16.5°, 19.7°, 20.2°, 21.0°, 21.9°, 23.4°, 25.7°, 28.0°, 30.0°, 31.0°, 32.5°, 33.6°, 34.5°, 36.1°, 37.7°, 39.8°, 40.8°, 42.3°, 43.0°, 44.2°, 46.3°, 47.8°, 48.8°, 50.6°, 52.5°, 55.5°, 56.3°, 58.7°
13X-zeolite	26.0°, 26.8°, 34.5°, 41.4°, 47.3°, 57.4°
Al_2O_3	16.2°, 18.1°, 25.6°, 30.3°, 32.9°, 35.4°, 36.7°, 38.9°, 40.5°, 43.4°, 44.9°, 48.5°, 57.3°, 67.5°

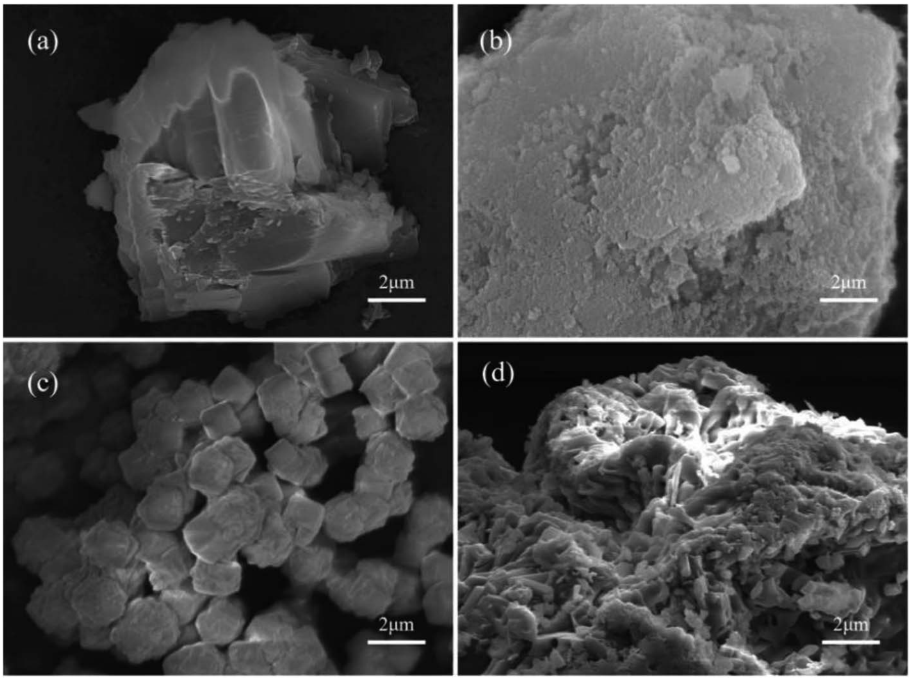

Fig. 3 SEM images of thermochemical heat storage materials composed of (a) $MgSO_4 \cdot 6H_2O$, (b) MA-1 ($MgSO_4 \cdot 6H_2O/Al_2O_3$), (c) MZ-2 ($MgSO_4 \cdot 6H_2O$/13X-zeolite) and (d) MPSA-3 ($MgSO_4 \cdot 6H_2O$/poly(sodium acrylate)).

discharge process. The $MgSO_4 \cdot 6H_2O$ content of MA-1, MZ-2, MPSA-3 is about 56%. During the preparation process the hygroscopic additives could retard the aggregation of $MgSO_4 \cdot 6H_2O$. The surface texture of $MgSO_4 \cdot 6H_2O$, MA-1, MZ-2 and MPSA-3 were tested by nitrogen adsorption–desorption. The BET specific surface area, pore volume and average pore size are provided in Table 3. These textural parameters were automatically obtained from the nitrogen adsorption–desorption measurements, which were carried out on a Quantachrome QDS-30 analyzer. The specific surface area value was obtained based on the equation: $S_w = V_m \times \lambda N/V_0$ (BET method);[36] where S_w is the specific surface area; V_m is the monolayer adsorption volume in the standard state; λ is the adsorbate molecular cross-sectional area, where the adsorbate molecule here is nitrogen gas; $\lambda = 0.162\ nm^2$; N is the Avogadro constant (6.02×10^{23}); and V_0 is the standard molar volume of adsorbate (22.4 $cm^3\ mol^{-1}$). The pore volume was obtained by a single-point adsorption process. The average pore size was obtained from the BJH method.[37] Because of the introduction of different hygroscopic additives, the specific surface areas of MA-1 (213 $m^2\ g^{-1}$) and MZ-2 (281 $m^2\ g^{-1}$) are higher than those of MPSA-3 (65 $m^2\ g^{-1}$) and $MgSO_4 \cdot 6H_2O$ (16 $m^2\ g^{-1}$). Combined with the SEM and XRD characterization results, it could be concluded that high specific surface area is another important factor for the nanoscale dispersion of $MgSO_4 \cdot 6H_2O$.

Table 3 Textural parameters of hygroscopic nanoadditive modified thermochemical materials

Samples	Surface area ($m^2\ g^{-1}$)	Pore volume ($mL\ g^{-1}$)	Average pore size (nm)
MA-1	213	0.19	2.19
MZ-2	281	0.16	2.37
MPSA-3	65	0.02	1.51
$MgSO_4 \cdot 6H_2O$	16	0.04	2.81

3.2 Heat storage performance testing of magnesium sulfate based thermochemical materials

The results of the heat storage performance tests of $MgSO_4 \cdot 6H_2O$, MA-1, MZ-2 and MPSA-3 are shown in Fig. 4. The related reaction is $MgSO_4 \cdot 6H_2O = MgSO_4 + 6H_2O$. The conversion rate is lower for pure magnesium sulfate, which is only 28% after 30 min of hydration. And the reaction heat of $MgSO_4 \cdot 6H_2O$ is only about 325 kJ kg^{-1} (Fig. 4a). Fig. 4b shows the heat storage performance of Al_2O_3-promoted $MgSO_4 \cdot 6H_2O$. It can be seen that $MgSO_4$ has completely reacted and the energy density of MA-1 could reach 1305 kJ kg^{-1}. The energy density of MZ-2 rises to a higher value (1411 kJ kg^{-1}, Fig. 4c) compared to the poly(sodium acrylate) modified $MgSO_4 \cdot 6H_2O$ sample MPSA-3 (1100 kJ kg^{-1}, Fig. 4d). The conversion reactions of MA-1, MZ-2 and MPSA-3 are fully completed. The respective conversion rates reach 100%, which are much higher than for pure magnesium sulfate. Compared with previous research,[24,26] when 13X-zeolite is used as the additive in this work, the energy density of MZ-2 ($MgSO_4 \cdot 6H_2O$/13X-zeolite; 1411 kJ kg^{-1}) could be 1.3 and 2.2 times higher than in previous research (1090 kJ kg^{-1}; 648 kJ kg^{-1}; magnesium sulfate content: 15%; impregnation method), reported in ref. 24 and 26, respectively. These results could be attributed to the materials preparation method and higher content of $MgSO_4 \cdot 6H_2O$ (56%) in the composite materials. In

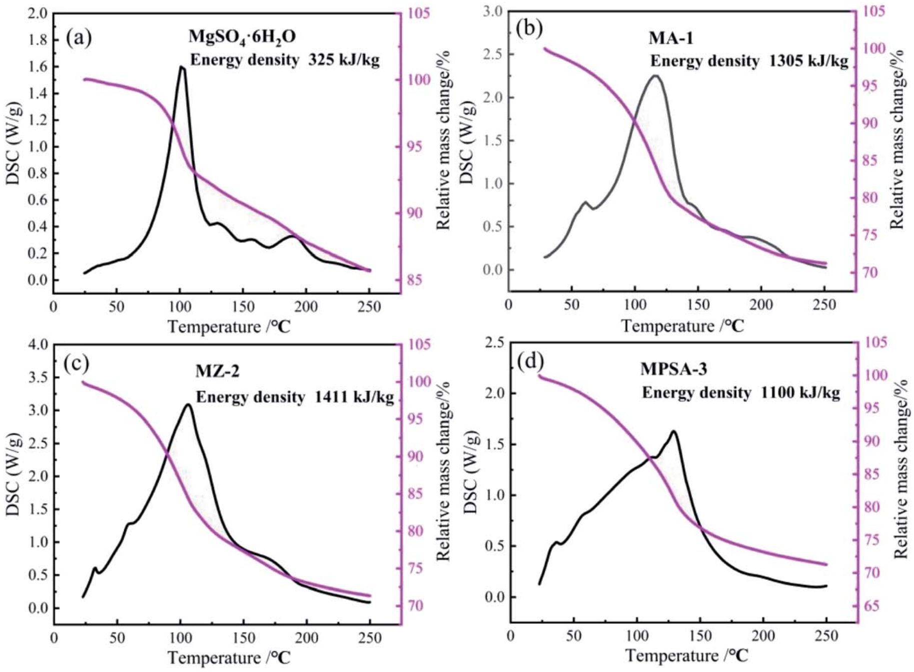

Fig. 4 TG-DSC curves of the samples: (a) $MgSO_4 \cdot 6H_2O$, (b) MA-1 ($MgSO_4 \cdot 6H_2O/Al_2O_3$), (c) MZ-2 ($MgSO_4 \cdot 6H_2O$/13X-zeolite) and (d) MPSA-3 ($MgSO_4 \cdot 6H_2O$/poly(sodium acrylate)) after 30 min of hydration.

this work, a hydrothermal method is used to prepare the composite materials and with this approach the material particles generated could be smaller and the mixed ratio could be well controlled. The heat storage performance test indicates that drawing poly(sodium acrylate), 13X-zeolite and nano-Al_2O_3 into magnesium sulfate hexahydrate gives a dramatically enhanced reaction rate for $MgSO_4$ and water vapor under the same hydration reaction conditions. The reason lies in the hygroscopic properties of the additives that make H_2O adsorption easier so more water molecules come into contact with the reaction interface on $MgSO_4$. The reason for the higher energy density of the modified materials is the higher specific surface area (Table 3), which improves the particle dispersion of $MgSO_4 \cdot 6H_2O$ and enlarges the contact area for water molecules. When the particle size is reduced to the nanoscale, the surface atoms would notably increase and a large number of dangling bonds would be formed, which could lead to improved thermodynamic properties.[38,39] It could be concluded that small nanoparticles could provide a greater contribution to energy density enhancement.

Tables 4–7 show the DSC analysis and results of the kinetic parameter calculations for $MgSO_4 \cdot 6H_2O$, MA-1, MZ-2 and MPSA-3 that include the heating rate, peak temperature and related functions. Fig. 5a–d show the linear fitting curve of the modified Arrhenius's equation and the reaction activation energy, which is calculated by the Kissinger method.[35] For $MgSO_4 \cdot 6H_2O$ the decomposition activation energy is the highest among the synthesized thermochemical materials and reaches 36.8 kJ mol^{-1} (Fig. 5a). However, hygroscopic additives make the endothermic reaction easier and decrease the activation energy (Fig. 5b–d). After adding Al_2O_3, 13X-zeolite and poly(sodium acrylate), the activation energies decrease to 28.5 kJ mol^{-1}, 32.4 kJ mol^{-1} and 22.3 kJ mol^{-1}, respectively. This proves that the addition of hygroscopic additives could remarkably decrease the difficulty of the heat storage reaction. According to the SEM results in Fig. 3a–d, this reduction in activation energy may relate to the change in particle size of $MgSO_4 \cdot 6H_2O$. As the $MgSO_4 \cdot 6H_2O$ particle size becomes smaller from big bulk (Fig. 3a) to nanoparticles (Fig. 3b–d) the

Table 4 DSC analysis and the results of the kinetic parameter calculations of $MgSO_4 \cdot 6H_2O$

Heating rate β (K min^{-1})	Peak temperature T (K)	$1/T \times 1000$ (K^{-1})	$\ln \beta/T^2$
5	374.3	2.67165	−10.24068
10	389.8	2.56542	−9.62868
15	407.6	2.45339	−9.31252
20	413.1	2.42072	−9.05165

Table 5 DSC analysis and results of the kinetic parameter calculations of MA-1 ($MgSO_4 \cdot 6H_2O/Al_2O_3$)

Heating rate β (K min^{-1})	Peak temperature T (K)	$1/T \times 1000$ (K^{-1})	$\ln \beta/T^2$
5	354.3	2.82247	−10.13085
10	378.0	2.64550	−9.56720
15	392.3	2.54907	−9.23600
20	400.7	2.49563	−8.99069

Table 6 DSC analysis and results of the kinetic parameter calculations of MZ-2 ($MgSO_4 \cdot 6H_2O$/13X-zeolite)

Heating rate β (K min^{-1})	Peak temperature T (K)	$1/T \times 1000$ (K^{-1})	$\ln \beta/T^2$
5	358.0	2.79330	−10.15163
10	379.1	2.63783	−9.57301
15	389.5	2.56739	−9.22168
20	400.5	2.49688	−8.98970

Table 7 DSC analysis and results of the kinetic parameter calculation for MPSA-3 ($MgSO_4 \cdot 6H_2O$/poly(sodium acrylate))

Heating rate β (K min^{-1})	Peak temperature T (K)	$1/T \times 1000$ (K^{-1})	$\ln \beta/T^2$
5	361.4	2.76702	−10.17053
10	383.0	2.61097	−9.59348
15	408.4	2.44858	−9.31644
20	419.7	2.38265	−9.08335

average value of the activation energy becomes about 0.75 times lower than that of $MgSO_4 \cdot 6H_2O$. It can be inferred that the microstructure and kinetic behavior have some relationship and the reaction activation energy is an important parameter for the heat storage reaction and could change perceptibly with different materials.

Fig. 6a and b show the water vapor adsorption testing of the mass transfer properties of $MgSO_4 \cdot 6H_2O$, MA-1, MZ-2 and MPSA-3, respectively. The adsorption curves of all of the samples show rapid rises for the stages of water adsorption and saturated water adsorption. These two stages exactly correspond to the water vapor mass transfer during the hydration reaction, which is attributed to physical/chemical adsorption accompanied by an exothermic and rapid increase in water adsorption and the adsorption balance. The water vapor saturated adsorption amount of MZ-2 is the highest among the samples (Fig. 6b), and the adsorption rate is also higher (Fig. 6a). This may be due to two factors: the hygroscopic porous structure of the 13X-zeolite and the nano-dispersion of $MgSO_4 \cdot 6H_2O$. All these factors are advantageous to water adsorption. When hygroscopic additives are composited with $MgSO_4 \cdot 6H_2O$, the adsorption rate is obviously affected. The adsorption rate of the poly(sodium acrylate) modified composite material MPSA-3 is the highest. Furthermore, highly dispersed $MgSO_4 \cdot 6H_2O$ provides enhanced water vapor adsorption. The composited material MZ-2 shows high water vapor adsorption (almost twice the adsorption amount of pure $MgSO_4 \cdot 6H_2O$, Fig. 6b) even though the content is only about half (56%). Enhanced water adsorption exhibits efficient mass transfer, which will improve the hydration reaction. For the thermal conductivity (Fig. 6c), adding Al_2O_3, 13X-zeolite and poly(sodium acrylate) could also change the heat transfer property of $MgSO_4 \cdot 6H_2O$, and meet the requirement for efficient utilization of thermal energy. Now, in order to promote the matching degree and future application of these materials, the heat transfer behavior of the $MgSO_4$-based

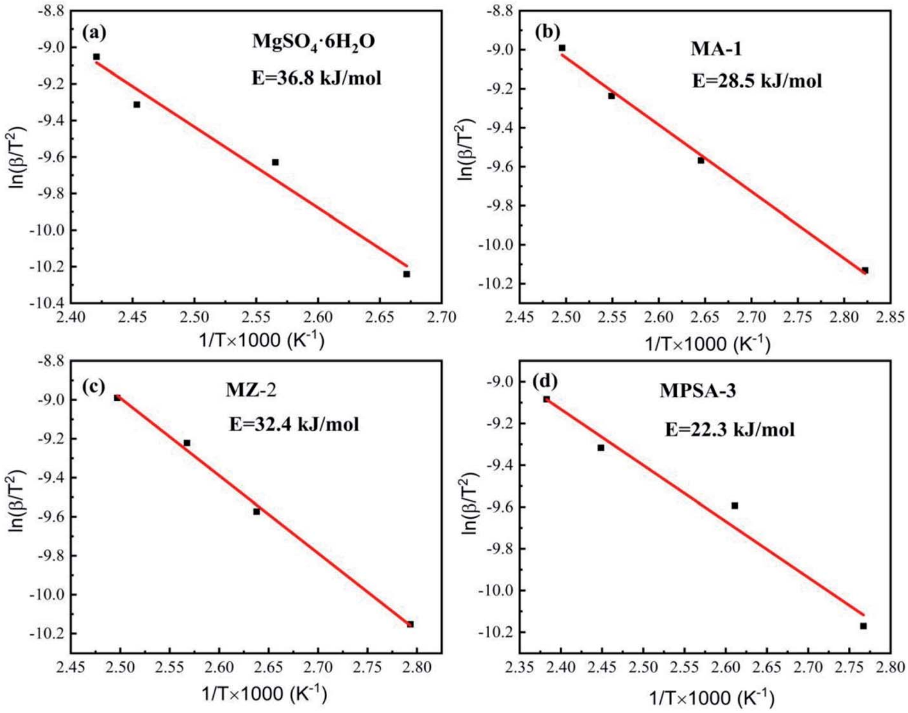

Fig. 5 Activation energy of the dehydration reaction of (a) $MgSO_4 \cdot 6H_2O$, (b) MA-1 ($MgSO_4 \cdot 6H_2O/Al_2O_3$), (c) MZ-2 ($MgSO_4 \cdot 6H_2O$/13X-zeolite) and (d) MPSA-3 ($MgSO_4 \cdot 6H_2O$/poly(sodium acrylate)).

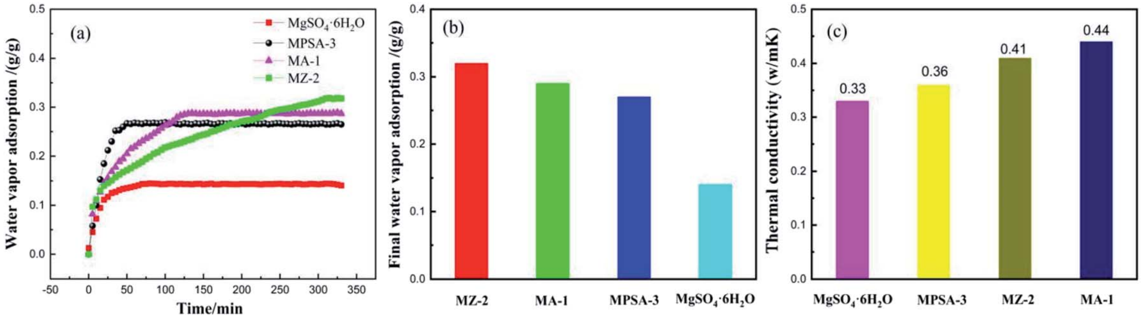

Fig. 6 (a) Water vapor adsorption; (b) the saturated adsorption amount; (c) thermal conductivity of $MgSO_4 \cdot 6H_2O$, MA-1 ($MgSO_4 \cdot 6H_2O/Al_2O_3$), MZ-2 ($MgSO_4 \cdot 6H_2O$/13X-zeolite) and MPSA-3 ($MgSO_4 \cdot 6H_2O$/poly(sodium acrylate)).

composite heat storage materials in stainless steel reactor was simulated.

3.3 Numerical simulations for heat transfer behavior of magnesium sulfate based composite heat storage material in the reactor

Fig. 7a–d show the numerical simulation temperature curves of the contact face in different areas of the reactor when the heat storage materials $MgSO_4 \cdot 6H_2O$, MA-1, MZ-2 and MPSA-3 are respectively packed in the reactor. All the temperature–time curves show a rapid upward trend in the initial temperature and a stable final temperature. This reflects the heat transfer process in the reactor, which consists of two stages. In the first stage the exothermic heat of reaction is higher than the heat elimination by the environment, leading to an endothermic and quick temperature rise of the reactor. The second is the heat balance stage: the exothermic heat of reaction is equal to the heat dissipation by the environment, meaning there is no temperature change.

Fig. 7a shows the core temperature T_{1c} of $MgSO_4 \cdot 6H_2O$ (40 °C) in the center of the reactor. The core temperature is higher

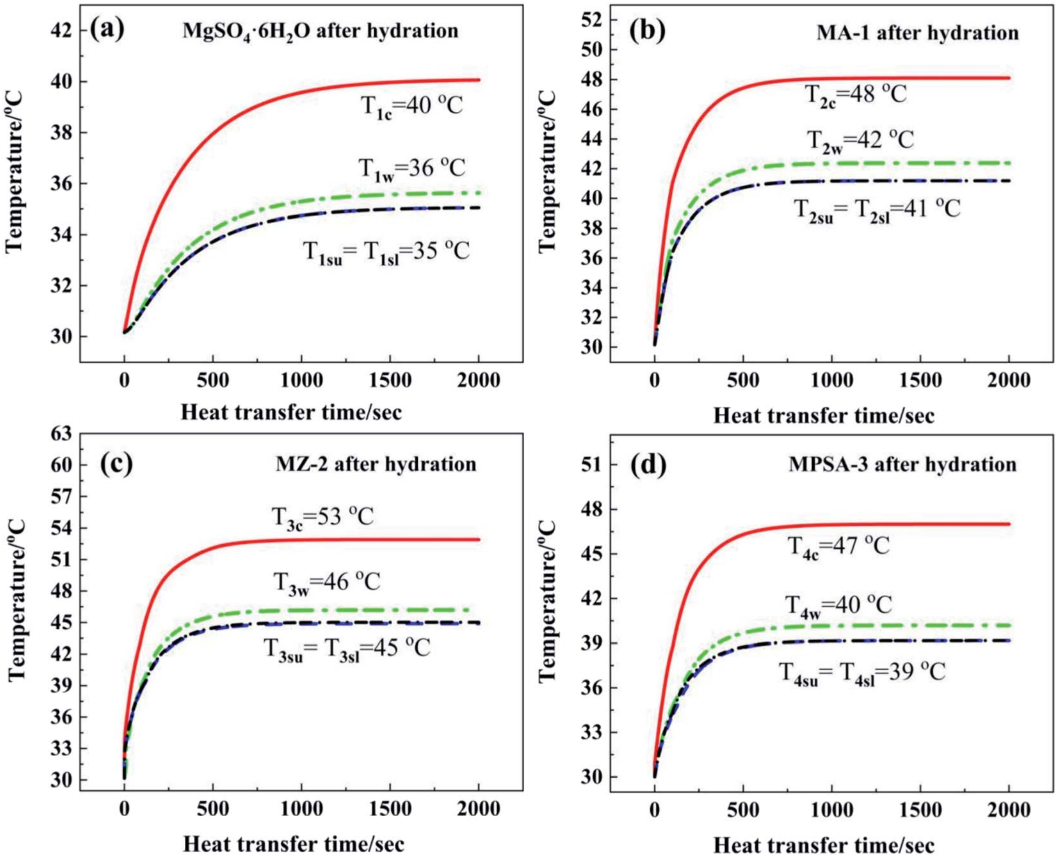

Fig. 7 Numerical simulations of temperature–time curves in the reactor: (a) $MgSO_4 \cdot 6H_2O$, (b) MA-1 ($MgSO_4 \cdot 6H_2O/Al_2O_3$), (c) MZ-2 ($MgSO_4 \cdot 6H_2O$/13X-zeolite) and (d) MPSA-3 ($MgSO_4 \cdot 6H_2O$/poly(sodium acrylate)) after the hydration reaction.

than the temperature in other positions of the reactor, which is due to the lower thermal conductivity of the materials. Under the same heat dissipation conditions, this causes higher thermal resistance in the direction of reaction heat transferred along the perpendicular from the reactor center to the inner wall. The inner wall temperature T_{1w} in the reactor was 36 °C. The difference between temperatures T_{1c} and T_{1w} was 4 °C. By comparison, the temperature gradients from the reactor center to the lower surface and upper surface of the heat storage material were a little higher than that from the reactor center to the inner wall (difference in temperature between T_{1c} and T_{1su} and T_{1sl}: 5 °C). The characteristic temperature distribution in the reactor was a high-temperature area in the center of the reactor and a low-temperature area near the reactor wall. The average temperature T_{1sl} of the interface between N_2 gas with water vapor and $MgSO_4 \cdot 6H_2O$ at the lower surface (35 °C) was equal to the average temperature T_{1su} of the upper surface (35 °C). After 1500 s the reactor could reach heat balance and the temperature stayed the same. In summary, the heat dissipation capacity of the bottom layer material was as good as that of the upper layer, and the released thermal energy was mainly transferred through the side wall of the reactor.

Fig. 7b–d show the temperature–time curves of the interface between the hygroscopic additive modified heat storage materials MA-1, MZ-2 and MPSA-3 and the reactor, respectively. It can be observed that the temperature of the material center and the contact surface between the heat storage material and the reactor could reach a heat balance when the reactions were sustained for about 850 s, 880 s, and 1000 s, respectively (Fig. 7b, c and d). Compared with the pure material $MgSO_4 \cdot 6H_2O$ (where the time required for heat balance is 1500 s, Fig. 7a), the composite material takes less time to reach heat balance, the heat transfer rate is faster and the exothermic temperature is higher than those of $MgSO_4 \cdot 6H_2O$. Among them, the core temperature T_{3c} of MZ-2 (Fig. 7c) is the highest, which can reach 53 °C, 13 °C higher than that of $MgSO_4 \cdot 6H_2O$. The reactor inner wall temperature T_{3w} is 10 °C higher than that of $MgSO_4 \cdot 6H_2O$ (Fig. 7a). The temperature at the lower surface (T_{3sl}) and upper surface (T_{3su}) of MZ-2 is also 10 °C higher than that of $MgSO_4 \cdot 6H_2O$. The exothermic temperatures at the heat balance stage in different interfaces of the other two materials are MA-1: $T_{2c} = 48$ °C, $T_{2w} = 42$ °C, $T_{2sl} = T_{2su} = 41$ °C (Fig. 7b) and MPSA-3: $T_{4c} = 47$ °C, $T_{4w} = 40$ °C, $T_{4sl} = T_{4su} = 39$ °C (Fig. 7d).

Fig. 8 shows a comparison of the numerical simulation and experimental temperature data for heat storage materials in the reactor. It can be seen that the simulated and experimental temperatures (T_c, T_w, T_{sl} and T_{su}) of the materials are almost equivalent. This indicates that the numerical simulation of the heat transfer process was accurate and extremely valuable for

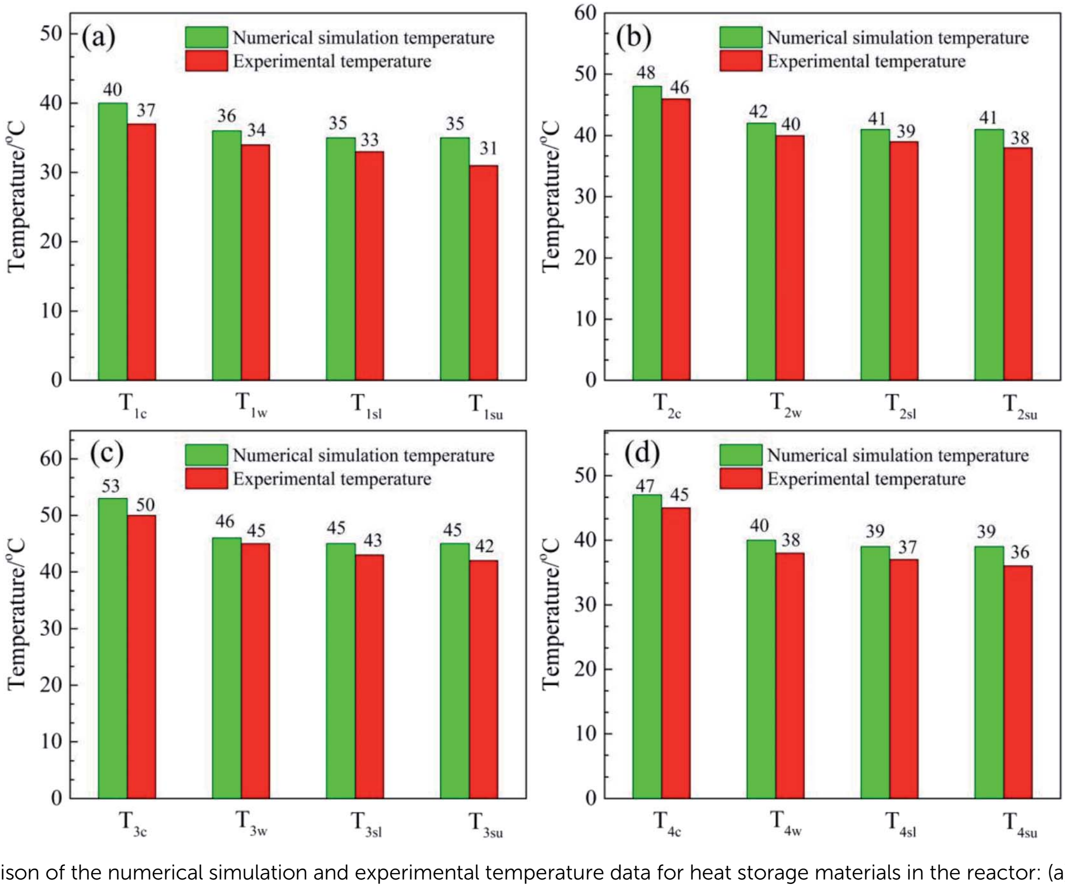

Fig. 8 Comparison of the numerical simulation and experimental temperature data for heat storage materials in the reactor: (a) $MgSO_4 \cdot 6H_2O$, (b) MA-1 ($MgSO_4 \cdot 6H_2O/Al_2O_3$), (c) MZ-2 ($MgSO_4 \cdot 6H_2O$/13X-zeolite) and (d) MPSA-3 ($MgSO_4 \cdot 6H_2O$/poly(sodium acrylate)) after the hydration reaction.

future material and reactor design. The results of the numerical simulation of the heat transfer process prove that the heat release and heat transfer properties of the hygroscopic additive modified composites (MA-1, MZ-2 and MPSA-3) are better than those of the pure material ($MgSO_4 \cdot 6H_2O$) in a stainless steel reactor.

The physical model used for the chemical heat storage material is a cylindrical stainless-steel reactor (Fig. 1a). On the basis of which, the heat transfer process is investigated and a numerical calculation mesh 3D model is established (Fig. 1b). And then the energy conservation equation is solved based on the finite volume method to simulate the heat transfer process in the reactor. Fig. 9 shows the temperature distribution for heat storage materials in the reactor for (a) $MgSO_4 \cdot 6H_2O$, (b) MA-1, (c) MZ-2 and (d) MPSA-3 after the hydration reaction. It can be seen from Fig. 9a–d that as the reaction progressed for 100 seconds, the temperature in the center of the reactor where the sample was located gradually rose and could reach above 40 °C except for $MgSO_4 \cdot 6H_2O$. Because of the low thermal conductivity and heat concentration of the materials, the central heating rate of the samples was faster and the core temperature was higher than those of other interfaces in the reactor. As the reaction proceeded and after 500 s the heat was gradually released in the reactor and started to transfer from the center of the heat storage material to the surroundings, which caused a rearrangement of the temperature and finally reached heat balance. And the temperature of the hygroscopic additive modified composited materials rose faster than that of the pure material. The whole temperature evolution showed the dynamic change in temperature in the heat release process of the reactor, which provided an advanced strategy for thermal energy utilization and the subsequent synthesis of heat storage materials and the optimal design of the reactor.

4. Conclusions

In this paper, a hydrothermal method was used to synthesize a hygroscopic additive: super-absorbent polymer material (poly(sodium acrylate)), 13X-zeolite and nano-aluminum oxide (nano-Al_2O_3) modified magnesium sulfate hexahydrate ($MgSO_4 \cdot 6H_2O$) composite thermochemical materials for low-temperature heat storage. After being composed with 13X-zeolite, nano-Al_2O_3 and poly(sodium acrylate), $MgSO_4 \cdot 6H_2O$ crystals are dispersed into nanoparticles (200–500 nm). The introduction of hygroscopic materials leads to a distinct decrease in activation energy for the heat storage reaction and an obvious increase in heat storage performance because of the excellent water adsorption properties and dispersal effect of the hygroscopic additives. The initial activation energy value and energy density of $MgSO_4 \cdot 6H_2O$ are 36.8 kJ mol^{-1} and 325 kJ kg^{-1}, respectively. For nano-Al_2O_3 modified composite material MA-1, the activation energy reaches 28.5 kJ mol^{-1} and the heat storage energy density is 1305 kJ kg^{-1}. But after modification by poly(sodium acrylate), the activation energy could decrease to

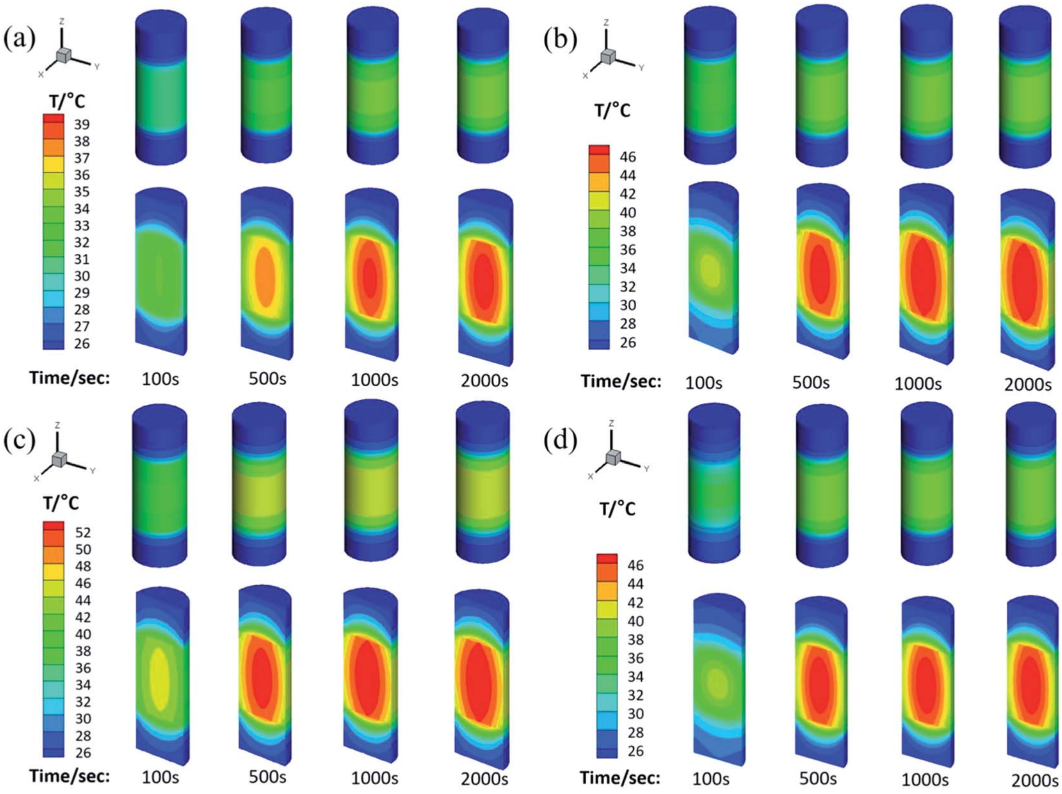

Fig. 9 The temperature distribution for heat storage materials in the reactor: (a) $MgSO_4 \cdot 6H_2O$, (b) MA-1 ($MgSO_4 \cdot 6H_2O/Al_2O_3$), (c) MZ-2 ($MgSO_4 \cdot 6H_2O$/13X-zeolite) and (d) MPSA-3 ($MgSO_4 \cdot 6H_2O$/poly(sodium acrylate)) after the hydration reaction.

22.3 kJ mol^{-1} (MPSA-3). This indicates that the activation energy can be reduced by expanding the specific surface area or improving the hydrophilicity of materials. Among the prepared materials, super-absorbent polymer material (poly(sodium acrylate)) modified composite material MPSA-3 shows a good heat storage energy density (1100 kJ kg^{-1}) and the lowest activation energy. 13X-zeolite modified composite material MZ-2 shows a lower activation energy (32.4 kJ mol^{-1}) and the highest heat storage energy density (1411 kJ kg^{-1}), which is 4.3 times higher than that of pure magnesium sulfate hexahydrate. According to a numerical simulation of the heat transfer, the involvement of hygroscopic additives could greatly change the temperature distribution in the reactor and efficiently export thermal energy to the outside thermal load side. The temperature values of experimental and numerical simulation are similar. This proves that the result of the numerical simulation is very close to the actual heat transfer behavior. This energy storage system could output thermal energy at around 50 °C and absorb heat in the range of 100–200 °C. This research proposes an advanced strategy combining thermochemical nanomaterials preparation followed by a material-reactor heat transfer numerical simulation, which will provide strong support for future materials and reactor design in the field of low-temperature thermal energy storage. Based on this research, the focus of the next step should be the size-controlled preparation of thermochemical materials and an investigation of the heat transfer behavior at the micro- and nanoscale and reactor design.

Author contributions

This research was conceived and designed with the participation of all the authors. Shijie Li and Xiangyu Yang contributed equally to this work. Shijie Li: conceptualization, writing – original draft, funding acquisition; Xiangyu Yang: resources; data curation; writing – review & editing; Lisheng Deng and Yongchun Fu: visualization, formal analysis; Mingjun Pang and Ti Dong: validation; Lingna Sua: investigation, Shang Jiang and Yisong Yu: supervision and funding acquisition. All authors have read and agreed to the published version of the manuscript.

Nomenclature

C_p	Specific heat capacity (J kg^{-1} K^{-1})
ρ	Gas density (kg m^{-3})
T	Temperature (K)
t	Time (s)
k	Thermal conductivity coefficients (W m^{-1} K^{-1})
r	Cylinder material model radius (m)
φ	Central angle
z	Cylinder material model height (m)
R	Reactor radius (m)
ε	Emissivity
σ	Stefan–Boltzmann's constant (W m^{-2} K^{-4})
f	Outside low temperature object
E	Activation energy (kJ mol^{-1})
T_{1c}	Core temperature of $MgSO_4 \cdot 6H_2O$ in reactor (°C)
T_{1w}	Inner wall temperature of reactor with $MgSO_4 \cdot 6H_2O$ (°C)
T_{1sl}	Lower surface temperature of $MgSO_4 \cdot 6H_2O$ in reactor (°C)
T_{1su}	Upper surface temperature of $MgSO_4 \cdot 6H_2O$ in reactor (°C)
T_{2c}	Core temperature of MA-1 in reactor MA-1 (°C)
T_{2w}	Inner wall temperature of reactor with MA-1 (°C)
T_{2sl}	Lower surface temperature of MA-1 in reactor (°C)
T_{2su}	Upper surface temperature of MA-1 in reactor (°C)
ϕ	Reactor diameter (mm)
h	Reactor height (mm)
β	Heating rate (K min^{-1})
R	Molar gas constant (J mol^{-1} K^{-1}) in Arrhenius's equation
A	Pre-exponential factor
α	Dehydration conversion rate
T_c	Core temperature of material in reactor (°C)
T_w	Inner wall temperature of reactor (°C)
T_{sl}	Lower surface temperature of material in reactor (°C)
T_{su}	Upper surface temperature of material in reactor (°C)
S_w	Specific surface area (m^2 g^{-1})
V_m	Monolayer adsorption volume at standard state (cm^3)
λ	Adsorbate molecular cross-sectional area (nm^2)
N	Avogadro constant (6.02×10^{23})
V_0	Standard molar volume of adsorbate (22.4 cm^3 mol^{-1})
T_{3c}	Core temperature of MZ-2 in reactor (°C)
T_{3w}	Inner wall temperature of reactor with MZ-2 (°C)
T_{3sl}	Lower surface temperature of MZ-2 in reactor (°C)
T_{3su}	Upper surface temperature of MZ-2 in reactor (°C)
T_{4c}	Core temperature of MPSA-3 in reactor (°C)
T_{4w}	Inner wall temperature of reactor with MPSA-3 (°C)
T_{4sl}	Lower surface temperature of MPSA-3 in reactor (°C)
T_{4su}	Upper surface temperature of MPSA-3 in reactor (°C)
w	Reactor wall thickness (mm)

Conflicts of interest

There are no conflicts to declare.

Acknowledgements

This work is supported by the Key-Area Research and Development Program of Guangdong Province (Grant No. 2020B0202010004); the National Natural Science Foundation of China (Grant No. 22008237); The Scientific and Technological Innovation Programs of Higher Education Institutions in Shanxi (through the Grant No. 201802097 and 2019L0745), and the Datong Applied Basic Research (2019166).

References

1 A. Gil, M. Medrano, I. Martorell, A. Lázaro, P. Dolado, B. Zalba and L. F. Cabeza, *Renewable Sustainable Energy Rev.*, 2010, **14**, 31.
2 N. Armaroli and V. Balzani, *Angew. Chem., Int. Ed.*, 2007, **46**, 52.

3 V. A. Salomoni, C. E. Majorana, G. M. Giannuzzi, A. Miliozzi, R. D. Maggio, F. Girardi, D. Mele and M. Lucentini, *Sol. Energy*, 2014, **103**, 303.
4 L. Miró, M. E. Navarro, P. Suresh, A. Gil, A. I. Fernández and L. F. Cabeza, *Appl. Energy*, 2014, **113**, 1261.
5 C. Mano and A. Thongtha, *J. Renewable Mater.*, 2021, **9**(3), 495.
6 A. Kardam, S. S. Narayanan, N. Bhardwaj, D. Madhwal, P. Shukla, A. Verma and V. K. Jain, *RSC Adv.*, 2015, **5**, 56541.
7 A. Shkatulov and Y. Aristov, *RSC Adv.*, 2017, **7**, 42929.
8 M. Rothensteiner, A. Bonk, U. F. Vogt, H. Emeriche and J. A. V. Bokhoven, *RSC Adv.*, 2017, **7**, 53797.
9 S. J. Li, H. Y. Huang, X. X. Yang, Y. Bai, J. Li, N. Kobayashi and M. Kubota, *Appl. Therm. Eng.*, 2018, **128**, 706.
10 X. X. Yang, H. Y. Huang, Z. H. Wang, M. Kubota, Z. H. He and N. Kobayashi, *Chem. Phys. Lett.*, 2016, **644**, 31.
11 S. J. Li, H. Y. Huang, J. Li, N. Kobayashi, Y. Osaka, Z. H. He and H. R. Yuan, *RSC Adv.*, 2018, **8**, 8199.
12 T. Yan, R. Z. Wang, T. X. Li, L. W. Wang and I. T. Fred, *Renewable Sustainable Energy Rev.*, 2015, **43**, 13.
13 P. Pardo, A. Deydier, Z. Anxionnaz-Minvielle, S. Rougé, M. Cabassud and P. Cognet, *Renewable Sustainable Energy Rev.*, 2014, **32**, 591.
14 H. Ishitobi, K. Uruma, M. Takeuchi, J. Ryu and Y. Kato, *Appl. Therm. Eng.*, 2013, **50**, 1639.
15 H. Ogura, T. Yamamoto and H. Kage, *Energy*, 2003, **28**, 1479.
16 D. A. Sheppard, M. Paskevicius and C. E. Buckley, *Chem. Mater.*, 2011, **23**, 4298.
17 K. Kyaw, T. Shibata, F. Watanabe, H. Matsuda and M. Hasatani, *Energy Convers. Manage.*, 1997, **38**, 1025.
18 K. Posern and C. Kaps, *Thermochim. Acta*, 2010, **502**, 73.
19 W. Wongsuwan, S. Kumar, P. Neveu and F. Meunier, *Appl. Therm. Eng.*, 2001, **21**, 1489.
20 M. Kubota, S. Matsumoto and H. Matsuda, *Appl. Therm. Eng.*, 2019, **150**, 858.
21 L. Farcot, N. L. Pierrès, B. Michel, J. F. Fourmigué and P. Papillon, *J. Energ. Storage*, 2018, **20**, 109.
22 A. Malley-Ernewein and S. Lorente, *Int. J. Heat Mass Transfer*, 2019, **130**, 1299.
23 Y. M. Luo, J. J. Rui, W. Xu, J. Q. Peng, X. H. Zhe, N. P. Li and Y. L. Ding, *Energy Storage Sci. Technol.*, 2021, **10**, 1273.
24 G. Whiting, D. Grondin, S. Bennici and A. Auroux, *Sol. Energy Mater. Sol. Cells*, 2013, **112**, 112.
25 U. R. Ata, K. Muhammad and M. S. Zheng, *J. Energy. Storage*, 2019, **26**, 101026.
26 S. Hongois, F. Kuznik, P. Stevens and J. J. Roux, *Sol. Energy Mater. Sol. Cells*, 2011, **95**, 1831.
27 C. Xu, Z. B. Yu, Y. Y. Xie, Y. X. Ren, F. Ye and X. Ju, *Appl. Therm. Eng.*, 2018, **129**, 250.
28 M. Kubota, N. Horie, H. Togari and H. Matsuda, *Annual Meeting of Japan Society of Refrigerating and Air Conditioning Engineers*, Tokai University, Japan, 2013.
29 Y. Wang and M. D. Levan, *J. Chem. Eng. Data*, 2009, **54**, 2839.
30 S. Wei, L. Zhang, L. Li and R. L. Lee, *Adsorption*, 2009, **15**, 497.
31 I. Gul, S. M. Khan, T. Mehmood, Z. Ahmad and H. Shah, *Microsc. Res. Tech.*, 2020, **83**(6), 1.
32 Y. Qiang, Y. H. Xie, Y. Qi, P. Wei, H. K. Shi, C. Geng and H. C. Liu, *Sol. Energy*, 2020, **201**, 523.
33 M. Minale, Z. L. Gu, A. Guadie, Y. Li, Y. Meng and X. J. Wang, *Chemosphere*, 2021, **272**, 129902.
34 T. Shiga, Y. Hirose, A. Okada and T. Kurauchi, *J. Appl. Polym. Sci.*, 2010, **44**(2), 249.
35 M. Kubota, S. Matsumoto, H. Matsuda, H. Y. Huang, Z. H He and X. X. Yang, *Adv. Mater. Res.*, 2014, **953–954**, 757.
36 *GB/T 19587-2004: Determination of the specific surface area of solids by adsorption using the BET method*.
37 J. Z. Fang, P. Li, L. G. Zhang and P. Xue, *J. Ningxia Univ., Nat. Sci. Ed.*, 2012, **33**, 195.
38 B. X. Wang, L. P. Zhou and X. F. Peng, *Int. J. Thermophys.*, 2005, **27**, 139.
39 L. J. Chen, R. Q. Zou, W. Xia, Z. P. Liu, Y. Y. Shang, J. L. Zhu, Y. X. Wang, J. H. Lin, D. G. Xia and A. Y. Cao, *ACS Nano*, 2012, **6**, 10884.